

# The Etched Hourglass Nebula MyCn18: II A Spatio-Kinematic Model

Aditya Dayal<sup>1,2</sup>, Raghvendra Sahai<sup>2</sup>, Alan M. Watson<sup>3</sup>, John T. Trauger<sup>2</sup>, Christopher J. Burrows<sup>4</sup>, Karl R. Stapelfeldt<sup>2</sup>, John S. Gallagher III<sup>5</sup>

## ABSTRACT

We have observed MyCn18, a young Planetary Nebulae with HST/WFPC2 and presented the observational results in an earlier paper (Paper I). Here we present a detailed spatial/kinematical model of H $\alpha$  emission from the nebula. We model the hourglass-shaped nebular lobes as thin-walled structures in the shape of modified paraboloids. Variations in the H $\alpha$  surface brightness with radius imply abrupt changes in the exponent of the power-law gas density in the hourglass walls. These density variations might reflect temporal variations in the mass-loss rate of the progenitor AGB star. Alternatively, they may be a result of the complex interaction between the fast and slow winds. From the H $\alpha$  surface brightness variations we infer that the nebula is density bounded everywhere, except in the vicinity of the dense waist. We derive a total mass of  $0.013 M_{\odot}$  for the walls of the ionized nebula and an upper limit of  $0.006 M_{\odot}$  for the mass in the interior. This appears to be a small fraction of the total mass ejected in the AGB phase. The nebular kinematics are well modeled with a radial velocity field where velocity increases with latitude. The density and velocity structures derived from our model are consistent with general predictions of the interacting winds hypothesis for planetary nebula formation.

*Subject headings:* planetary nebulae: individual (MyCn18), stars: AGB and post-AGB, stars: mass-loss, circumstellar matter

## 1. Introduction

Multi-wavelength observations from the ground and space show that the majority of Planetary Nebulae (PN) are not spherical (e.g. Balick et al. 1998, Sahai & Trauger 1998, Aaquist & Kwok

---

<sup>1</sup>IPAC/JPL, MS 100-22, California Institute of Technology, Pasadena, CA 91125

<sup>2</sup>Jet Propulsion Laboratory, MS 183-900, California Institute of Technology, Pasadena, CA 91109

<sup>3</sup>Instituto de Astronomía, Universidad Nacional Autónoma de México, J. J. Tablada 1006, 58090 Morelia, Michoacán, México

<sup>4</sup>Space Telescope Science Institute, 3700 San Martin Drive, Baltimore, MD 21218

<sup>5</sup>Department of Astronomy, University of Wisconsin, Madison, 475 N. Charter Street, Madison, WI 53706

1996, Corradi & Schwarz 1995). Some are simply elliptical, bipolar or “butterfly-shaped” (i.e. axially symmetric), while others show more complex point-symmetric structures. Additionally, many sources also show multiple rings, arcs, jets or ansae. Over the last two decades the generalized interacting stellar winds (GISW) scenario (e.g. Kwok, Purton & Fitzgerald 1978, Balick 1987, Frank et al. 1993) has been established as the “standard model” for explaining the shapes of PNe from a hydrodynamical standpoint. In GISW models, the hydrodynamical interaction of a fast PN wind with a slower, equatorially concentrated red giant wind is shown to reproduce a variety of axisymmetric shapes. While the GISW models appear to have been at least qualitatively successful in reproducing PNe morphologies, a quantitative measure of their success depends on how well their predictions match up with observationally inferred physical parameters. In this paper we present a detailed spatio-kinematic model of the etched hourglass nebula, MyCn18, and provide physical parameters (density and velocity structure) which may better constrain hydrodynamical models of this source, or similar hourglass-shaped sources.

We have obtained images of MyCn18 with the Wide Field & Planetary Camera 2 (WFPC2) on the *Hubble Space Telescope*. The images, which show a remarkable hourglass shaped nebula, have been presented in Sahai et al. (1999) – hereafter Paper I. Here, we use the H $\alpha$  image (Fig. 1) along with existing ground-based spectra to construct a 3-dimensional spatial and kinematical model of the nebula. By comparing these data to our model results we are able to constrain the shape, dimensions and tilt of the nebula, infer densities along each line of sight and deproject observed velocities to obtain a complete 3-D model of the density and velocity structure. Similar spatio-kinematic models of bipolar PN have been presented recently by, for e.g., Miranda, Guerrero & Torrelles, J. M. (1999), Lopez et al. (1998) and Miranda (1995). While these previous studies focussed primarily on the more unusual kinematical properties of a few PNe, the results from the current study are intended to provide better constraints for radiation gas dynamic models which attempt to understand the actual formation and evolution of such nebulae.

The observational details and description of the morphology of MyCn18 are given in Paper I. In §2 we develop the detailed spatio-kinematic model for the nebula in order to infer its shape and structure, and constrain the mass of ionized gas. In §3 we discuss the implications of our model results for theories of formation and evolution of this PN. Finally, in §4 we present a summary of the main results from this paper.

## 2. A Spatio-Kinematic Model of the Nebula

We have constructed a 3-D spatio-kinematic model to investigate the shape of the nebula walls and the density, and kinematics of the emitting gas. Our 3-D model grid consists of a large number (currently  $6.4 \times 10^7$ )  $0.046''$ -size volume elements (cells), specified in cartesian coordinates. Within this grid the volume emissivity ( $\text{erg s}^{-1} \text{cm}^{-3}$ ) and velocity fields are specified independently, and are free to vary as a function of radius and/or latitude. The volume emissivity is subsequently used to infer the density and/or temperature distribution by assuming

an appropriate source function for the emission mechanism under consideration (e.g. line emission from ionized gas, dust-scattered light or dust thermal emission). Assuming a radial velocity field for the expanding nebula, surface brightness maps are obtained at multiple projected velocities spanning an emission-line. The model image at any particular projected velocity is obtained by numerically integrating the emissivity from each cell along the line of sight (*los*) that shares that velocity, for each point on the projected surface of the model nebula. Thermal line broadening is expected to be a small fraction of the total line width (see §2.4) and is ignored. The nebular emission is assumed to be optically thin. For continuum emission processes, a similar integration is performed but the velocity field is ignored.

While the high resolution HST images constrain the overall geometry and emissivity field quite well, kinematical data are also very useful as they provide information on the orientation of the nebula, the nebular dimensions along the *los*, and dynamical timescales. In this paper we compare a model long-slit spectrum of MyCn18 with the kinematical data of Corradi & Schwarz (1993). Used together, the images and long-slit spectrum yield a well-constrained “best-fit” model which is determined via an iterative process. A schematic of the geometry adopted for our models is presented in Fig. 2. As in Paper I, we adopt a distance of 2.4 kpc to MyCn18.

## 2.1. Shape

We find that the shape of the nebular walls can be adequately described as a truncated paraboloid close to the star and a truncated cone further away (Fig. 2). Simple paraboloids are unable to reproduce the observed degree of collimation of the lobes. As we are primarily interested in obtaining the 3-D density/velocity structure of the nebula (e.g.  $n_e \sim f(R, \theta)$ ), we have used the simplest geometry which provides a good match to the data. Other parametrizations might provide equally good matches to the data, but they too would, presumably, yield similar density/velocity laws. Our model does not attempt to describe the more complex inner region of the nebula, where we find the inner hourglass and the two rings.

The parameters that fix the shape of the hourglass walls are the latitude  $\phi_1$  of transition from the paraboloid to the cone, the latitude  $\phi_2$  of the end of the cone, the slope  $\phi_3$  of the cone, the semi-height  $H$  of the hourglass, and the waist radius  $R_w$  (refer to Fig. 2). The model nebula is assumed to be symmetric about the  $z$  axis, and tilted by an angle  $\theta$  with respect to the *los*. The shape of the walls in our model is defined by Equations 1–3:

$$x^2 + y^2 = \left( \frac{z_p}{\tan^2 \phi_1} - \frac{R_w^2}{z_p} \right) z + R_w^2 \text{ cm}, \quad |z| \leq z_p \quad (1)$$

$$\sqrt{x^2 + y^2} = \frac{z}{\tan \phi_3} - z_p \left( \frac{1}{\tan \phi_3} - \frac{1}{\tan \phi_1} \right) \quad |z| > z_p \quad (2)$$

where

$$z_p = H \frac{(\tan\phi_3/\tan\phi_2) - 1}{(\tan\phi_3/\tan\phi_1) - 1} \quad (3)$$

The radial distance from the hourglass center,  $R = \sqrt{x^2 + y^2 + z^2}$ , and the latitude,  $\phi = \tan^{-1}(z/\sqrt{x^2 + y^2})$ .

Discounting the complex region within  $1''$  of the center and the microstructure (mottlings, etchings) in the lobes, the source morphology can be divided into regions according to whether the *los* intersects the walls of a single lobe once or twice or the walls of both lobes (Fig. 1). The apparent dimensions of these regions, for e.g., the observed height-to-width ratio of the lobes, allow us to constrain the shape parameters of the nebula (defined above) and its inclination. The wall thickness,  $dR$ , is constrained by comparing angular intensity slices which cut across the walls of the model and  $H\alpha$  images (Fig. 3). Making the walls too thick decreases the brightness contrast between the faint interior regions (where the *los* runs almost perpendicular to walls) and the brighter, limb-brightened edges (where the *los* runs tangentially through a long column of wall material). We obtain a reasonable fit to the data with a wall thickness of  $(1.6 \pm 0.8) \times 10^{16}$  cm. We assume that the wall thickness is constant throughout the nebula; however we are unable to rule out variations within the range given by these uncertainties, particularly due to projection effects arising from the large tilt of the nebula to the *los*.

The large surface brightness ratio between the interior and edge-brightened region indicates that the walls of the nebula have a significantly higher emission measure than the region they enclose. See §2.3 for estimates of the density in the nebula.

## 2.2. Kinematics

The kinematics play an indispensable role in uniquely determining the 3-D structure from a 2-D image. Under an assumption about the intrinsic velocity field (radial, for example), the observed velocity from any point on the nebula along a *los* determines the location of that point in the *los* direction. Hence, the shape parameters can be determined only through an iterative procedure using both images and kinematical data as constraints. To compare with the long-slit observations of CS93 (their Fig. 10), our models calculate average-velocity versus position curves. We assume that the nebula expands radially outwards and that the velocity at each point in the hourglass walls follows a radial power law.

The nebula is tilted such that the south-eastern lobe (Fig. 1, top lobe) is closer to the observer than the north-western lobe (Fig. 1, bottom lobe). Moving away from the nebular center along the major axis into the south-eastern lobe, we first encounter a large column density of material from the far-side wall of the lower (red-shifted) lobe, where the radial velocity vectors point away from us. This explains the red-shifted bulge that extends for about  $3''$  above the center. Beyond  $3''$ , the emission is solely from the upper (blue-shifted) lobe. As the distance from the center

increases the radial velocity vectors continue to tip towards the *los* to the nebula and the average velocity becomes more blue-shifted. The shape of the lower half of the position–velocity diagram has an analogous explanation.

Our model kinematical curves are shown superposed on the data of CS93, in Fig. 4. While they fit the data rather well overall, there are some clear discrepancies also, particularly in the inner regions (see §2.4). In the CS93 data positive DEC increments imply decreasing declination (H. Schwarz, private communication) and although the CS93 plot refers to the [NII] $\lambda$ 6586 line, it is reasonable to assume that it reflects the velocity field of the bulk of the ionised gas, given the very close spatial correspondence of the [NII] and H $\alpha$  emissions. The model curves shown are of the form:

$$V_r = 24 \text{ km s}^{-1} (R/1.3 \times 10^{17} \text{ cm})^n. \quad (4)$$

and the best-fit appears to be obtained with an exponent,  $n=0.6\pm0.4$ . Since  $R$  increases monotonically with latitude in the hourglass walls, the expansion velocity also increases with latitude, from about  $10 \text{ km s}^{-1}$  at the lowest latitudes to roughly  $40 \text{ km s}^{-1}$  at  $60^\circ$  (see Table 1). A similar increase of expansion velocity with latitude has been found for the molecular gas in the cylindrical walls of the bipolar planetary nebula IC4406 (Sahai et al. (1991)). The corresponding dynamical timescales range from 1000–2500 yr.

Using the spatial and kinematical constraints we infer an inclination of  $\theta \approx 30\text{--}35^\circ$  (w.r.t. the *los*) for the nebula, with the S–E lobe tilted towards the observer. The hourglass shape parameters are estimated to be:  $R_w = 0.55''$  ( $2 \times 10^{16} \text{ cm}$ ),  $H = 8.0''$  ( $2.9 \times 10^{17} \text{ cm}$ ),  $\phi_1 = 44^\circ$ ,  $\phi_2 = 62^\circ$ , and  $\phi_3 = 85^\circ$ , with uncertainties of about  $\pm 5\%$ .

### 2.3. Wall Emissivity and Density of Ionized Gas

If the H $\alpha$  emission is optically thin (as we assume here) the surface brightness at any point in the nebula is proportional to the volume emissivity ( $j_{\text{H}\alpha} \text{ erg s}^{-1} \text{ cm}^{-3}$ ) integrated along the line of sight. Therefore, once the tilt of the nebula and its geometry (thus, path lengths along *los*) are fixed, surface brightness variations can be used to determine  $j_{\text{H}\alpha}(R)$ .

Fig. 5 shows the observed H $\alpha$  surface brightness  $S_{\text{H}\alpha}$  against the projected distance along the major axis of the nebula,  $\xi$ . Four regions can clearly be distinguished. The innermost region within  $0''.6$  shows a gently increasing surface brightness. The surface brightness then drops roughly as  $\xi^{-3.5}$  out to  $3''.6$ . At this point, which roughly corresponds to the mottled region, the surface brightness increases as  $\xi^3$  out to about  $5''.6$ . Finally, the surface brightness drops roughly as  $\xi^{-4}$  beyond  $5''.6$ . The corresponding variations in the H $\alpha$  volume emissivity with radial distance are found to be:

$$j_{\text{H}\alpha} = 5.14 \times 10^{-16} (R/3.0 \times 10^{16})^{-4.0} \quad 2.0 \times 10^{16} \leq R(\text{cm}) < 3.0 \times 10^{16} \quad (5)$$

$$j_{\text{H}\alpha} = 6.49 \times 10^{-19} (R/1.3 \times 10^{17})^{-4.0} \quad 3.0 \times 10^{16} \leq R(\text{cm}) < 1.3 \times 10^{17} \quad (6)$$

$$j_{H\alpha} = 6.49 \times 10^{-19} (R/1.3 \times 10^{17})^{+3.0} \quad 1.3 \times 10^{17} \leq R(\text{cm}) < 2.0 \times 10^{17} \quad (7)$$

$$j_{H\alpha} = 2.36 \times 10^{-18} (R/2.0 \times 10^{17})^{-3.0} \quad 2.0 \times 10^{17} \leq R(\text{cm}) \quad (8)$$

The emissivity in the innermost region ( $R < 3.0 \times 10^{16}$  cm, which corresponds to a  $z$ -height of  $7.2 \times 10^{15}$  cm) follows the same power law as that in the next, outer region (Eqn. 6), but is scaled up by a factor of 2.25 in order to fit the observed brightness of Ring 1.

The  $H\alpha$  emissivity is related to the proton and electron densities by the equation:  $j_{H\alpha}/n_p n_e = 3.56 \times 10^{-25}$  erg cm<sup>3</sup> s<sup>-1</sup> (Case B,  $T_e = 10,000$  K; Osterbrock 1989). Assuming that heavy elements contribute a negligible proportion of the electrons, we can calculate the radial variations in density from:

$$n_e(R) \approx 1.68 \times 10^{12} \sqrt{j_{H\alpha}(R)} \text{ cm}^{-3} \quad (9)$$

where  $j_{H\alpha}(R)$  is given by Eqns. 5–8. Implicit in this derivation is the assumption that the filling factor in the nebular walls,  $\epsilon \sim 1$ . Since the densities derived here are in general agreement with those derived by CS93 using the SII 6716/6731 line ratio (thus independent of  $\epsilon$ ), we believe that this is a reasonable assumption.

Our “best-fit” model  $H\alpha$  image is given in Fig. 6. The densities in the model hourglass walls (derived from Eqns. 5–9) are given in Table 1 – they range about  $1350 \text{ cm}^{-3}$  at mid-latitudes ( $\phi = 34^\circ$ ,  $R = 1.3 \times 10^{17}$  cm) to greater than  $10^4 \text{ cm}^{-3}$  at low latitudes ( $\phi \lesssim 10^\circ$ ). CS93 derived electron densities ranging from  $10^4 \text{ cm}^{-3}$  in the center of the nebula to  $500 \text{ cm}^{-3}$  in the “faint outer lobes”; our model-derived densities appear to be in agreement with these values. By summing up over the entire nebula we find that the total mass of the ionized gas in the walls is approximately  $0.013 M_\odot$ . Our models successfully reproduce the observations (to within the noise level of the data) by assuming that all of the emission comes from the walls. We estimate that the densities inside the lobes of the nebula are at least a factor 5–10 lower than the lowest densities in the walls; i.e.  $n_e(\text{interior}) < 300 \text{ cm}^{-3}$ .

The similarity in radial profiles between the  $H\alpha$  and the F547M filters (Fig. 5) suggests that the latter is dominated by continuum emission from ionized gas. The total nebular continuum flux density,  $F_c$ , is related to the total  $H\alpha$  line intensity,  $F_{H\alpha}$ , by the ratio of emission coefficients:  $F_c/F_{H\alpha} = \gamma_\nu/(4\pi j_{H\alpha}) = 2.55 \times 10^{-15} \text{ Hz}^{-1}$  (using  $\gamma_\nu = 9 \times 10^{-40} \text{ erg s}^{-1} \text{ cm}^3 \text{ Hz}^{-1}$ ; Brown and Mathews 1970). This yields a total nebular continuum flux density,  $F_c = 9.5 \text{ mJy}$ , which compares well with our measured F547M flux density of  $9.8 \text{ mJy}$  (Paper I). We are thus able to match the F547M image also simply by a scaled version of the  $H\alpha$  model

## 2.4. Model limitations

As stated earlier, the geometry in the central regions of the hourglass is complex, and hard to fit with our simple hourglass model. Although our model provides a good fit to the data beyond about  $0''.6$ , Fig. 4 shows that it underestimates the emission within Ring 1 by orders of magnitude.

To investigate whether most the emission seen within Ring 1 is real, or contaminated by the wings of the PSF, we deconvolve the H $\alpha$  image using the Lucy-Richardson algorithm as implemented in IRAF-STSDAS, with a PSF generated by Tiny Tim (Krist & Hook 1997). We find that the deconvolution reduces the central intensity by about 40%, leading us to conclude that there *is* an additional component of ionized gas within Ring 1. The precise spatial distribution of material in this central component cannot be unambiguously determined. However, we can obtain a rough estimate of the its mass by assuming a particular geometry. (The inferred mass depends relatively weakly on the geometry.) If the material lies in a constant-density disk coplanar with the hourglass waist and the thickness of the disk is equal to the z-extent of the enhanced-density waist region ( $7.2 \times 10^{15}$  cm), the density is roughly  $1.6 \times 10^4$  cm $^{-3}$  and the mass  $\sim 1.2 \times 10^{-4} M_{\odot}$ . This represents about 1% of the total mass of ionised gas in the nebula.

The kinematical data comparison (Fig. 3) shows that our “best-fit” model curve fits the overall shape of the data quite well but there appear to be some clear discrepancies. For e.g., the model predicts more extreme velocities at positions  $\pm 1.5''$  from the center than the data. These discrepancies may be illustrative of deviations from our derived geometry and/or density law or due to deviations from a radial velocity field. (It is plausible that velocities in some regions of the hourglass are tangential rather than radially directed. For example, the etchings at higher latitudes suggest instabilities which may be produced by shear flows along the nebular walls.) Furthermore it is obvious from the comparison that the two lobes of the hourglass are not identical (unlike those in the model). Each model curve clearly fits one lobe better in some regions than the other lobe. However, we note that the deviations (between data and model) are relatively small ( $\lesssim 5$  km s $^{-1}$ ) when compared to the velocity resolution of the data,  $\Delta V \sim 35$  km s $^{-1}$  (CS93). Therefore, the model limitations notwithstanding, we believe that our hourglass model provides a reasonably well-determined fit to the *overall* density and velocity structure of MyCn18, and the results we obtain here can be used to compare with hydrodynamical model predictions. Higher spectral resolution, spatially resolved data will enable us to constrain the structure of MyCn18 even better.

### 3. Discussion

#### 3.1. Density and Velocity structure

Hydrodynamical models of interacting stellar winds show that the observational appearance of PNe depend strongly on a variety of initial conditions such as the equator-to-pole density contrast in the slow wind ( $e/p$ ), the steepness of the poleward decrease in the AGB wind density and the mass loss rates/velocities of the slow and fast winds. (e.g. Mellema & Frank 1995, Frank & Mellema 1994). Models with large  $e/p$  ratios and small ambient (red-giant) velocities produce prolate shells of swept-up gas with a pronounced bipolar shape, including a cusp at equator. A fast wind with velocity on the order of a few hundred km s $^{-1}$  would probably be adequate to produce

an hourglass shape. There appear to be no direct measurement of the fast wind in MyCn18, but the observations of Bryce et al. (1997) show faint knots of emission moving away (approximately along the major axis of the nebula) at velocities  $\sim 500 \text{ km s}^{-1}$ . The authors interpret these high velocity knots to be powered by a bipolar, rotating, episodic jet. However the knots may also represent fragments of the swept-up shell driven by the fast wind, as it breaks out of the AGB envelope along the lower density poles.

We have found no models in the literature that match the shape of MyCn18 in detail, such as its *very narrow waist* and *open* hourglass-shaped lobes. However, in models that predict hourglass-like, bipolar nebulae with *closed* lobes (e.g. Dwarkadas, Chevalier & Blondin 1996), the densities (expansion velocities) are highest (lowest) along the equator and decrease (increase) with increasing latitude. These results are consistent with our results for MyCn18 (see Table 1). The models of Dwarkadas, Chevalier & Blondin (1996), which use an asymmetric density profile for the slow AGB wind, show that the velocity field is *approximately* radial and velocities increase gradually with latitude (by about a factor of two going from  $30^\circ$  to  $60^\circ$  in their Fig. 3). The velocities we derive appear to be in close agreement with these. The increase in  $t_{dyn}$  with  $R$  (or latitude) suggests that the acceleration is higher at higher latitudes (assuming that all points along the shell have the same age) and that the exponent of the velocity power law will increase with time, as the PN evolves.

A comparison of our derived density law (Section §2.3) with the images of MyCn18 (Fig. 1) shows that (a) the transition from the smooth to the etched region of the hourglass walls occurs approximately where the density-variation changes from a radially-decreasing one to a radially-increasing one, and (b) the mottled emission occurs where the density-variation reverts back to being radially-decreasing. One explanation for the gradually increasing density in the hourglass walls in the vicinity of the etchings might be a corresponding variation in the slow AGB wind. In this case the dramatic *increase* in density with radius in the region of the etchings (i.e. offset= $3''.6$ - $5''.7$  in Fig. 5) implies a sharp *decrease* in the AGB mass-loss rate with time. Such a decrease might result from a thermal pulse in the AGB star (Blöcker 1995). The gap between the density breaks corresponds to a radial distance of about  $7 \times 10^{16} \text{ cm}$  or a timescale of  $\sim 2000 \text{ yr}$  on the AGB, assuming an AGB expansion velocity of  $10 \text{ km s}^{-1}$ . Alternatively, the higher density region (like the etchings themselves) may be produced by dynamical and/or thermal instabilities at the interface between the fast and slow winds in the higher latitude regions of the hourglass.

### 3.2. Ionization Bounded or Density Bounded?

Whether a PN is optically thick or optically thin to ionizing continuum photons (i.e. ionization bounded or density bounded) has important implications for estimates of total nebular mass, distance (when using the Shklovsky method) and Zanstra temperature (e.g. Pottasch 1980 and references therein; Kaler 1983). In principle we could use our OIII (highest excitation), NII and  $H\alpha$  (highest excitation) images to construct ratio maps to probe for the location of an ionization



front. If the front were contained in the walls of the nebula we would expect, for e.g., the NII/H $\alpha$  or NII/OIII ratios to increase sharply here. Unfortunately, we are unable to use the OIII images due to the poor signal-to-noise ratio it affords in the outer regions of the hourglass nebula. We have also constructed a NII/H $\alpha$  ratio map but find that due to projection effects it is impossible to see variations in the ratio across the walls of the nebula. Therefore, we employ a few other methods here and show that MyCn18 is for most part density bounded, i.e. that the ionized mass derived for the hourglass walls (§2.3) appears to represent the total mass in the hourglass.

**(i) Surface brightness fall-off** – If the walls of the hourglass nebula are ionization bounded, i.e. all the ionizing photons are trapped by the walls, then variations in the H $\alpha$  surface brightness of the wall with radial distance must reflect corresponding variations in the incident ionizing flux. The ionizing flux in the interior of a nebula decreases as  $e^{-\tau_\nu} R^{-2}$  due to absorption of photons and geometric dilution. However, as the interior of the hot, low-density lobes are likely fully ionized (e.g. Frank et al. 1993), the optical depths to lyman continuum photons here are probably very small,  $e^{-\tau_\nu} \sim 1$ .

At each point along the hourglass wall the number of ionizing photons absorbed per unit area depends on  $\theta_{\text{star}}$ , the angle between the local tangent to the wall and the radial vector to the central star (see Fig. 7). The emergent intensity depends on the angle between the local tangent and the  $los$ ,  $\theta_{los}$ , because of varying path lengths through the wall. Thus, if the walls are ionization bounded, the surface brightness should be proportional to  $R^{-2} \frac{\sin(\theta_{\text{star}})}{\sin(\theta_{los})}$ . For simplicity we restrict ourselves to the regions of the hourglass where the  $los$  intersects only one wall of the nebula ( $1''.8$  to  $5''.3$ ). In this region  $\frac{\sin(\theta_{\text{star}})}{\sin(\theta_{los})} \approx 0.37$  and roughly constant, and  $R$  is proportional to  $\xi$ . Consequently, the observed surface brightness would fall-off as  $\xi^{-2}$  (or slower) if the nebula were ionization bounded. Since the observed decrease of surface brightness is much steeper than  $\xi^{-2}$ , we conclude that the walls of the nebula are density bounded and the decrease in surface brightness implies that densities in the wall decrease with increasing  $R$ . However, this conclusion does not apply to the inner part of the nebula within  $R < 0''.6$  (or  $\xi < 0''.6$ ) where the surface brightness does not appear to decrease with radius.

**(ii) Observed H $\alpha$  Flux** – The rate at which ionizing photons are emitted by the 51000 K,  $L=990 L_\odot$  star (paper I),  $N_i$ , is approximately  $6.8 \times 10^{46} \text{ s}^{-1}$ . The total recombination rate (using the observed H $\alpha$  luminosity to infer the H $\beta$  luminosity and the case B recombination coefficient; Tables 4.1 and 2.1 Osterbrock 1989),  $N_r \sim 1.7 \times 10^{46} \text{ s}^{-1}$ . A ratio,  $N_i/N_r > 1$  suggests that the nebula (or some region thereof) is density bounded;  $N_i/N_r \sim 4$  that we obtain here implies an escape probability of about 0.8 and a wall optical depth of about 0.2 for ionizing photons, averaged over the nebula. It also suggests that optical depths in the Ly-series resonance lines are quite large, justifying our choice of Case B emission.

Having constructed the geometrical model, we can also use our derived wall emissivity

function,  $j_{H\alpha}(R)$ , to estimate the ratio ( $R_{i/r}$ ) at each point in the walls of the nebula. We find that below latitudes of about  $10^\circ$  the ratio is roughly unity but at higher latitudes it has values greater than 3. This result suggests that the nebula is ionization bounded at latitudes below  $10^\circ$  but density bounded at higher latitudes. Thus, we suspect that any neutral material, if it exists, may be concentrated along the equatorial plane. A word of caution needs to be added here: in the region of the etchings (latitude  $\geq 35^\circ$ ) where the local density is rising, the ratio  $R_{i/r}$  approaches 1, raising the possibility that the dense substructures here are actually ionization bounded.

(iii) **Neutral gas** – Finally, since ionization-bounded PNe usually have observable amounts of molecular material (e.g. Kastner et al. 1996, Zuckerman and Gatley 1988), non-detections in  $H_2$  and CO provide additional support that MyCn18 is mostly density bounded. Webster et al. (1988) did not detect emission from MyCn18 in vibrationally excited  $H_2$  at  $2.12\mu m$ . Even though  $H_2$  is generally shock-excited and not necessarily a good tracer of cold molecular gas there is a strong correlation between  $H_2$  and CO detections (Huggins et al. 1996). Furthermore, we were also unable to detect any CO J=1-0 line emission in MyCn18 in a sensitive search with the Swedish-ESO Submillimeter Telescope at La Silla, Chile (unpublished data). We suspect that any molecular material, if is present, may be too cold and/or diffuse and below the sensitivity of the observations that were made.

### 3.3. Total Nebular Mass

The ionized mass we derive ( $0.013 M_\odot$ ; §2.3) is a very small fraction of the total nebular mass expected to have been lost on the AGB. If the Hourglass Nebula was created by star with a typical initial mass  $\sim 1 M_\odot$ , and the central white dwarf has a typical mass of  $\sim 0.6 M_\odot$  (Liebert 1980), then the nebula contains about  $0.4 M_\odot$  of material. Since we inferred only the mass of ionized material in the walls of the hourglass, this value is probably a lower limit to the total ionized mass in the nebula. Could there be significant amounts of ionized gas inside or outside of the bright, high-density walls?

The upper limits imposed on the density in the interior of the lobes ( $n_e < 300 \text{ cm}^{-3}$ ; §2.3), allow us to derive a corresponding upper limit of  $6 \times 10^{-3} M_\odot$  for the total mass in the interior. Thus the total ionized mass in the walls/interior of the nebula may be as high as  $0.02 M_\odot$ , a number which falls within the large range of estimated PNe ionized masses (e.g. Zhang 1995, Aaquist & Kwok 1991). The diffuse  $H\alpha$  intensity immediately outside the dense walls of the nebula also indicates the presence of material outside the hourglass, in the progenitor AGB envelope. The existence of this material appears to be supported by the observed 6 cm intensity. Using the relation  $S_{6cm} \text{ (Jy)} = 1.29 \times 10^9 F_{H\alpha} \text{ (mW m}^{-2}\text{)}$  (Pottasch 1984; Osterbrock 1989), we estimate a 6 cm flux density of 50 mJy. This number is about a factor of two lower than the flux density measured by Milne (1979),  $S_{6cm} = 106 \pm 10 \text{ mJy}$  using the Parkes (CSIRO) 64m telescope. Since their beam was  $\sim 4'$  (HPBW), Milne's observations were probably more sensitive (than our

images) to the extended ionized material lying outside the walls of the hourglass. It is difficult to estimate the mass outside the hourglass directly from the  $H\alpha$  image because much of the diffuse intensity outside the walls may be due to scattering of wall  $H\alpha$  photons by dust grains. However, the surface brightness RMS from regions outside and away from the walls impose a limit on the AGB mass loss rate and ionized mass:  $\dot{M} \leq 6 \times 10^{-6} M_{\odot} \text{ yr}^{-1}$  and  $M \leq 0.03 M_{\odot}$  (assuming an outer radius of  $3.2 \times 10^{17} \text{ cm}$ ), if the material lying outside of the nebular walls is spherically distributed and follows an  $R^{-2}$  density law. Therefore, for a reasonable AGB mass loss rate there can be a significant amount of ionized gas outside of the hourglass walls (as expected for a density bounded nebula), but all the ionized material (both inside and outside the nebular walls – out to  $R = 3.2 \times 10^{17} \text{ cm}$ ) is clearly unable to account for “missing” mass. This result implies that either (a) a large fraction of the “missing mass” in MyCn18 is neutral or (b) that most of the “missing mass” is ionized, but the emission lies below our  $H\alpha$  sensitivity limit and extends much further out than  $R = 3.2 \times 10^{17} \text{ cm}$ .

Although there have been no detections of molecular gas in MyCn18, we cannot rule out the existence of a significant atomic component in this nebula. About 10 PNe have been detected in the HI 21 cm line but only 3 of these sources are detected in CO (Gussie & Taylor 1995, Huggins et al. 1996). Like the 7 objects which have appreciable atomic gas but not molecular gas, MyCn18 may also have a substantial amount of HI; however our analysis suggests that this neutral gas does not lie in the vicinity of the hourglass walls (except at the waist, where the nebula is ionization bounded). In estimating the composition of the “missing mass” it is difficult to ascertain the proportion of neutral/ionized gas in the extended nebula as this depends on the unknown location and shape of the ionization front.

It is important to note that the “missing mass” problem does not only affect MyCn18, but is more widespread. Most observations of molecular/ionized gas in PNe yield masses that are considerably lower than  $0.4 M_{\odot}$  (e.g. Zhang 1995, Dayal & Bieging 1996, Huggins et al. 1996), suggesting that the bulk of the AGB envelope is often below observational sensitivity limits. Based on typical AGB timescales of  $10^5 \text{ yr}$  (Habing 1996) and a constant expansion velocity of  $10 \text{ km s}^{-1}$ , we would expect AGB remnant envelopes to extend out to a distance of approximately  $3 \times 10^{18} \text{ cm}$ . We detect  $H\alpha$  emission in MyCn 18 out only to one-tenth of this distance. We conclude that a significant proportion of the “missing mass” lies in an extended envelope, whose surface-brightness is below our detection limits.

#### 4. Summary

In summary, we have constructed a spatio-kinematic model of the young planetary nebula MyCn18 to compare with our HST/WFPC2 images (Paper I) as well as existing ground-based spectra. Our primary results show: (1) The nebula is well modelled as an hourglass inclined  $\sim 30\text{--}35^\circ$  with respect to the line of sight, with the S–E (top) lobe tilted towards the observer. (2) The expansion velocity varies as  $R^{0.6 \pm 0.4}$ , implying that it increases with latitude; this suggests

that the nebula is relatively young. Dynamical timescales range from about 1,000 yr along the equator (or waist) to about 2,500 yr at the rim of the hourglass lobes. The density and velocity structure agree with general predictions of GISW models, even though these models do not address more complicated aspects of the source’s morphology. (3) We find that the total mass for the ionized gas in the hourglass walls is roughly  $0.013 M_{\odot}$  and impose an upper limit of  $0.006 M_{\odot}$  on material inside the walls. (4) The walls of the nebula are density-bounded at higher latitudes ( $\geq 10^{\circ}$ ) and ionization bounded near the waist of the hourglass. Changes in the surface brightness of H $\alpha$  with radius imply abrupt changes in the exponent of the power-law gas density in the hourglass walls. These might be the result of variations in the mass-loss rate of the progenitor AGB star, perhaps during a thermal pulse, or due to the complex interaction between the fast and slow winds. (5) The ionized mass we derive is a small fraction of the total mass that is expected to be lost during the AGB phase. Most of this mass probably lies in an extended envelope below our detection sensitivity.

This work was supported by NASA grant NAS 7-1260 to the WFPC2 IDT. We thank Vikram Dwarkadas for useful discussions on hydrodynamical model results and their interpretation. We also thank the referee for detailed comments, which helped improve upon an earlier draft of this paper. The research described in this paper was partially carried out by the Jet Propulsion Laboratory, California Institute of Technology, under a contract with NASA.

## REFERENCES

- Aaquist, O. B. & Kwok, S. 1991, ApJ, 378, 599
- Aaquist, O. B. & Kwok, S. 1996, ApJ, 462, 813
- Balick, B. 1987, AJ, 94, 671
- Balick, B., Alexander, J., Hajian, A. R., Terzian, Y., Perinotto, M. & Patriarchi, P. 1998, AJ, 116, 360
- Blöcker, T. 1995, A&A, 297, 727
- Brown and Mathews 1970, ApJ, 160, 939
- Bryce, M., Lopez, J.A., Holloway, A.J., & Meaburn, J. 1997 ApJ, 487, L161
- Corradi, R.L.M. & Schwarz, H.E. 1993, A&A, 268, 714
- Corradi, R.L.M. & Schwarz, H.E. 1995, A&A, 293, 871
- Dayal, A. & Bieging, J. H. 1996, ApJ, 472, 703
- Dwarkadas, V. V., Chevalier, R. A. & Blondin, J. M. 1996, ApJ, 457, 773

- Frank, A., Balick, B., Icke, V. & Mellema, G. 1993, *ApJ*, 404, L25
- Frank, A. & Mellema, G. 1994, *ApJ*, 430, 800
- Gussie, G. T. & Taylor, A. R. 1995, *MNRAS*, 273, 801
- Habing, H. J. 1996, *A&A Rev.*, 7, 97
- Huggins, P. J., Bachiller, R., Cox, P. & Forveille, T. 1996, *A&A*, 315, 284
- Kahn, F. D. & Breitschwerdt, D. 1990, *MNRAS*, 242
- Kaler, J. B. 1983, *ApJ*, 271, 188
- Kastner, J. H., Weintraub, D. A., Gatley, I., Merrill, K. M. & Probst, R. G. 1996, *ApJ*, 462, 777
- Krist, J. & Hook, R. 1997, *Tiny Tim User's Guide*
- Kwok, S., Purton, C.R., & Fitzgerald, P.M. 1978, *ApJ*, 219, L125
- Liebert, J. 1980, *ARA&A*, 18, 363
- Lopez, J. A., Meaburn, J., Bryce, M. & Holloway, A. J. 1998, *ApJ*, 493, 803
- Mellema, G. & Frank, A. 1995, *MNRAS*, 273, 401
- Milne, D. K. 1979, *A&AS*, 36, 227
- Miranda, L. F. 1995, *A&A*, 304, 531
- Miranda, L. F., Guerrero, M. A. & Torrelles, M. A. 1999, *AJ*, 117, 1421
- Osterbrock, D. E. 1989, in *Astrophysics of Gaseous Nebulae and Active Galactic Nucleii*, (Mill Valley : University Science Books)
- Pottasch, S. R., 1980, *A&A*, 89, 336
- Pottasch, S. R. 1984, in *Planetary Nebulae*, (Dordrecht : Reidel)
- Sahai, R., Wootten, A., Schwarz, H.E., Clegg, R.E.S. 1991, *A&A*, 251, 560
- Sahai, R. & Trauger, J.T. 1998, *AJ*, 116, 1357
- Sahai, R. et al. 1999, *AJ*, in press
- Webster, B. L., Payne, P. W., Storey, J. W. V. & Dopita, M. A. 1988, *MNRAS*, 235, 533
- Zhang, C. Y. 1995, *ApJS*, 98, 659
- Zuckerman, B. and Gatley, I. 1988, *ApJ*, 324, 501

Fig. 1.—  $H\alpha$  image of MyCn18 taken through the narrowband F656N filter. The plate scale is  $0''.0456/\text{pixel}$ , and the image covers an area  $22''.8 \times 22''.8$  ( $500 \times 500$  pixels). The linear streak in the upper right quadrant of the  $H\alpha$  image is due to imperfect removal of a cosmic-ray event. A logarithmic stretch and reverse grey-scale has been used in the image, and the maximum (black) and minimum (white) values of the surface brightness respectively are  $1.81 \times 10^{-11}$  &  $3.67 \times 10^{-15}$   $\text{erg s}^{-1} \text{cm}^{-2} \text{arcsec}^{-2}$ .

Fig. 2.— Schematic view of the geometrical structure of the nebula showing various model parameters.

Fig. 3.— Angular intensity cuts in the top and bottom lobes of the data and model  $H\alpha$  images (along arcs  $q'q$  and  $rr'$  in Fig. 6). For each lobe, the cut-center is located  $8''.5$  from the nebular center along the nebular axis in the opposite lobe. The cuts are  $0''.3$  wide, with a radius of curvature of  $12''.65$ . An offset angle of  $0^\circ$  corresponds to positions along  $q'q$  and  $rr'$  which lie on the nebular axis. At offset angles of  $\pm(15-20^\circ)$  the arcs intersect the bright walls of the nebula.

Fig. 4.— Position–Average velocity plot, showing data (from CS93) and models for four different radial velocity power-laws.

Fig. 5.— Radial intensity cuts from  $H\alpha$  & F547M images (data and model) taken along the nebular axis ( $*p$  &  $*p'$  in Fig. 6). The  $H\alpha$  cuts are averaged over a  $10^\circ$  wedge, F547M cuts are averaged over a  $20^\circ$  wedge.

Fig. 6.— Model  $H\alpha$  image displayed using a logarithmic stretch and reverse grey-scale as in Fig. 1; the dotted lines show curves defining the intensity cuts shown in Figs. 3 and 5.

Fig. 7.— A schematic showing the emission geometry for a point on the hourglass wall.  $TT'$  represents the tangent to the wall,  $ON$  is the normal to the wall.  $\bar{r}$  is the radially directed vector through the point.  $R$  is the radial distance to the point,  $\xi$  is the observed offset (§2.3) and  $\theta_{los}$  and  $\theta_{star}$  are as defined in the text (§3.2). The flux of ionizing photons incident on the wall is proportional to  $\sin(\theta_{star})$ . The emergent intensity is inversely proportional to  $\sin(\theta_{los})$ .

Table 1. Model densities, velocities and timescales

Latitude ( $\phi$ )	$R^a$ (cm)	$n_H^a$ (cm $^{-3}$ )	$V^{a,b}$ (km s $^{-1}$ )	$t_{dyn}^a$ (yr)
0°	$2.80 \times 10^{16}$	43,100	9.6	930
5°	$3.50 \times 10^{16}$	18,500	10.9	1,020
10°	$4.44 \times 10^{16}$	11,700	12.5	1,130
15°	$5.62 \times 10^{16}$	7,200	14.5	1,230
20°	$7.05 \times 10^{16}$	4,600	16.6	1,350
25°	$8.73 \times 10^{16}$	3,010	18.9	1,470
30°	$1.08 \times 10^{17}$	1,930	21.6	1,590
35° <sup>c</sup>	$1.36 \times 10^{17}$	1,440	24.6	1,760
40°	$1.69 \times 10^{17}$	2,000	28.1	1,920
45° <sup>c</sup>	$2.08 \times 10^{17}$	2,430	32.0	2,070
50°	$2.32 \times 10^{17}$	2,050	34.1	2,170
55°	$2.67 \times 10^{17}$	1,680	36.8	2,310
60°	$3.16 \times 10^{17}$	1,300	40.9	2,460

<sup>a</sup>Due to the finite thickness of the walls of the nebula the radial distance increases as each line of constant latitude traverses through the wall. Values given here are those at the mid-point of the wall along each line of latitude.

<sup>b</sup>“Best-fit” velocity law assumes radial field,  $V_r = 24 \text{ km s}^{-1} (R/1.3 \times 10^{17} \text{ cm})^{0.6}$ .

<sup>c</sup>Breaks in the density law occur at  $R = 1.3 \times 10^{17} \text{ cm}$ ,  $\theta \sim 34^\circ$ ,  $n_H = 1,350 \text{ cm}^{-3}$  and at  $R = 2.0 \times 10^{17} \text{ cm}$ ,  $\theta \sim 44^\circ$ ,  $n_H = 2,580 \text{ cm}^{-3}$ .





Fig. 1

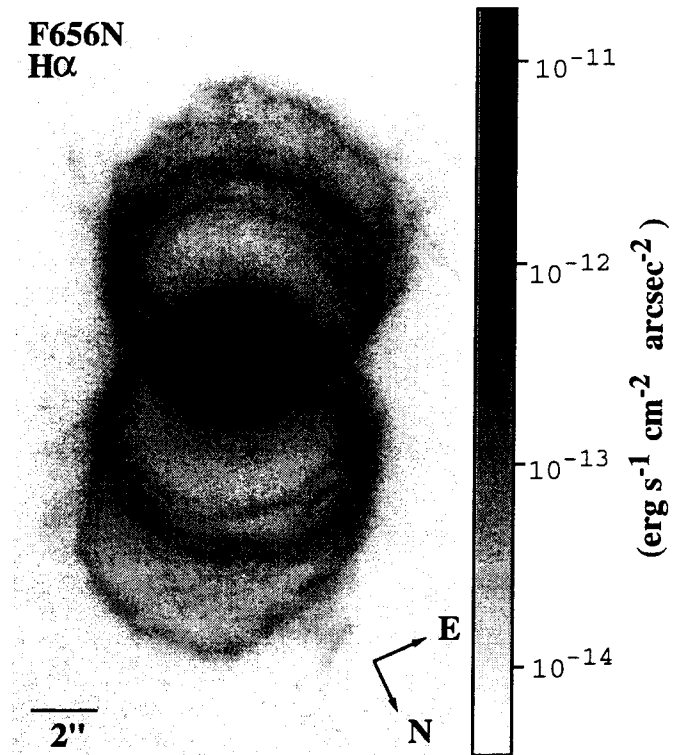


Fig. 2

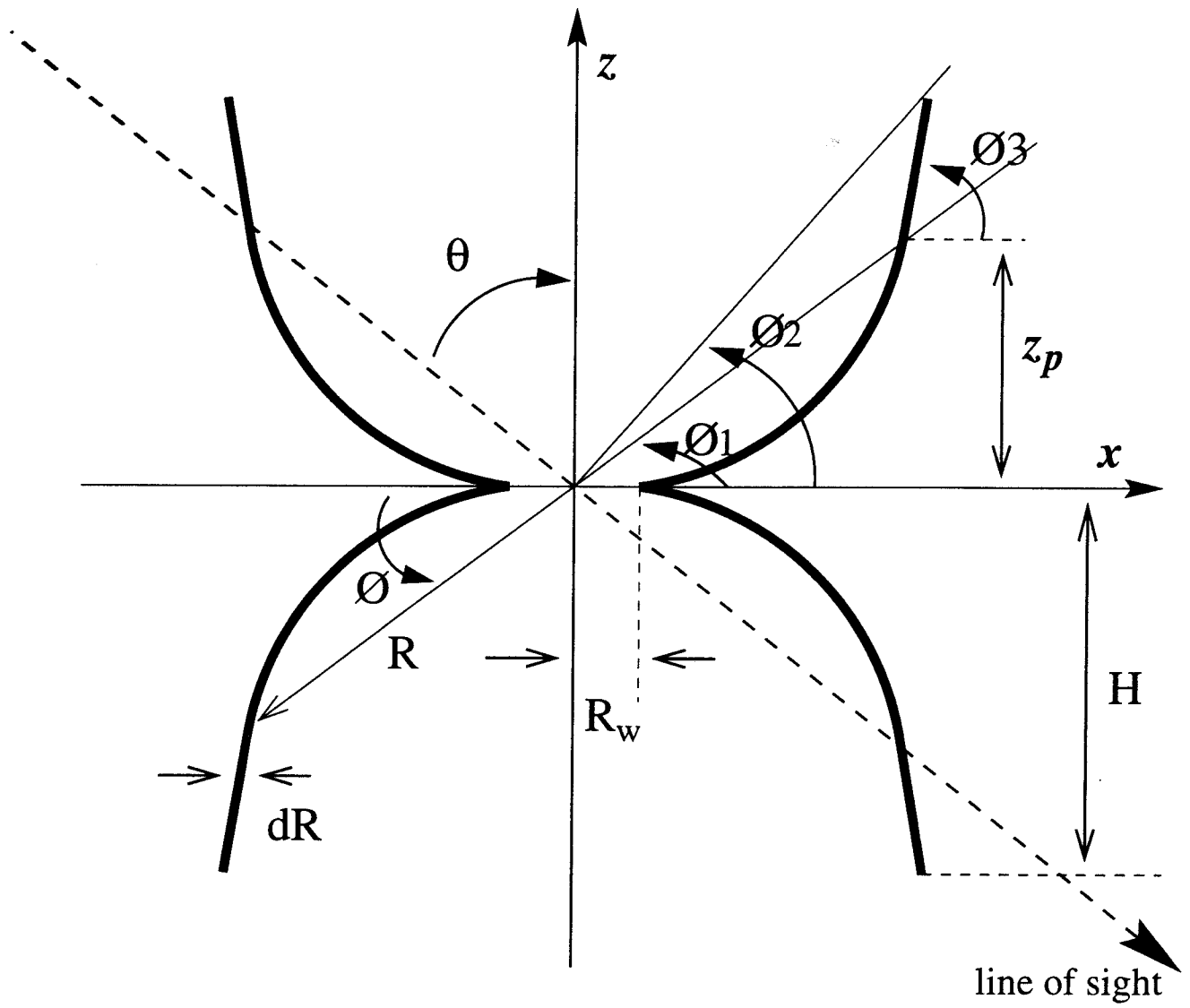


Fig. 3

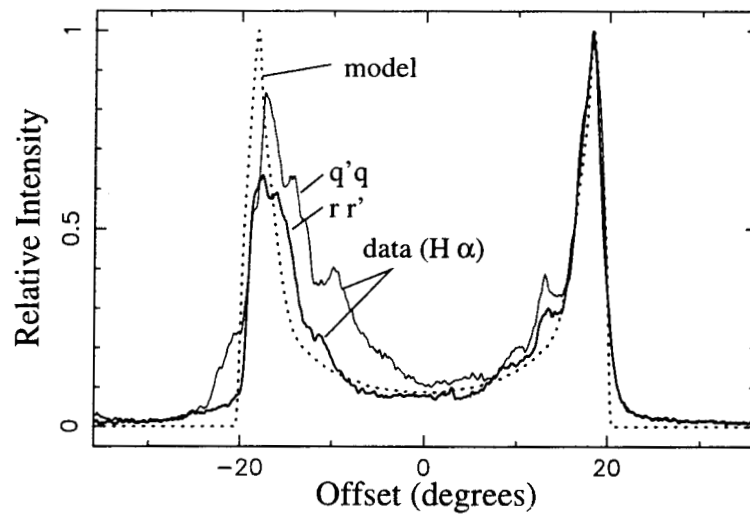


Fig.4

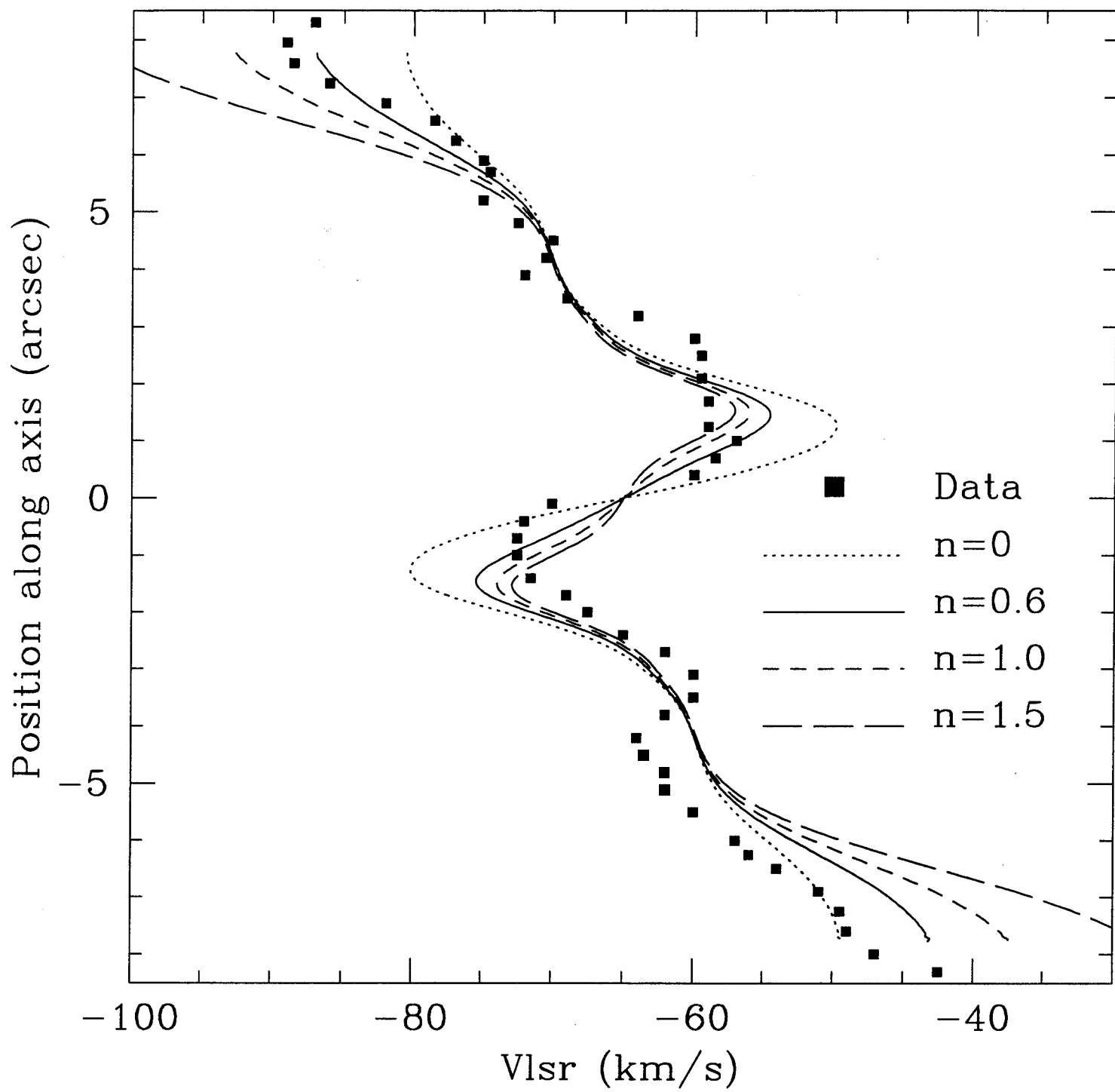


Fig. 5

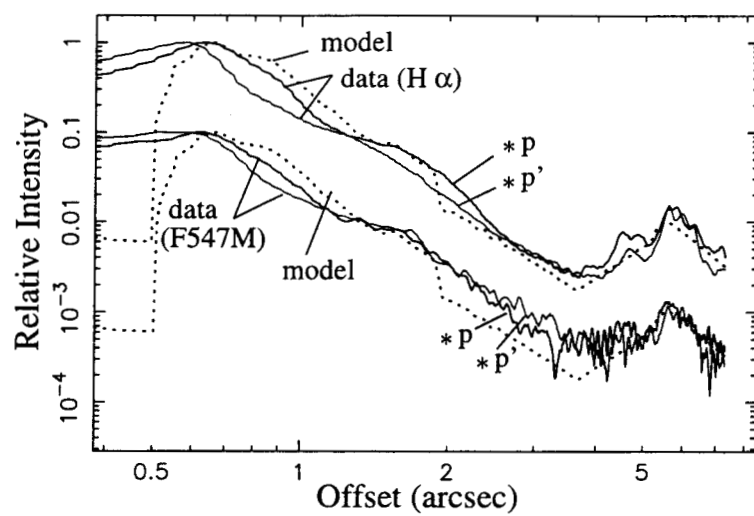


Fig. 6

Model H $\alpha$

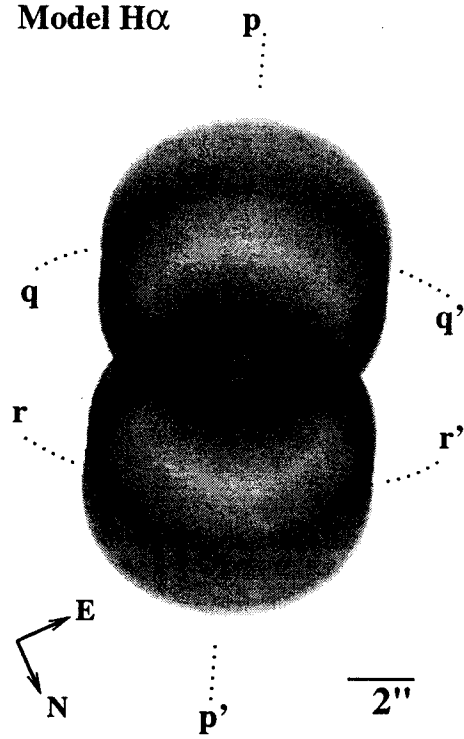


Fig. 7

